Journal of Materials Chemistry B

ROYAL SOCIETY OF CHEMISTRY

PAPER

View Article Online
View Journal | View Issue

Check for updates

Cite this: J. Mater. Chem. B, 2025, 13, 10500

Mineralized double-network hydrogels for the controlled release and improved stability of antimicrobial peptides

Yu Tian,[ac] Shixiong Zhang,[b] Wentao Zhai,[ac] Chenxi Duan,[ac] Donghua Zhang,[a] Jun Hu[bc] and Yi Zhang *[ac]

Received 19th May 2025,
Accepted 2nd August 2025

DOI: 10.1039/d5tb01186h

rsc.li/materials-b

Antimicrobial peptides (AMPs) have attracted considerable attention in chronic wound management and the prevention of implant-associated infections due to their excellent bactericidal activity, low toxicity, and great biocompatibility. However, their poor stability and uncontrolled release often result in transient efficacy, necessitating frequent administration. Developing a delivery system that ensures both sustained release and mechanical stability is crucial for the clinical translation of AMPs. To address these challenges, in this study, a Ca/P mineralized double-network (DN) hydrogel was developed, which consisted of a physically crosslinked polyvinyl alcohol (PVA) and a previously designed AMP termed IK3, to achieve controlled AMP release. The findings demonstrated that mineralization enhanced the structural integrity of the DN hydrogel while acting as a diffusion-regulating barrier to enable controlled and sustained IK3 release. *In vitro* antibacterial assays revealed sustained and potent antibacterial activity, with the mineralized hydrogel retaining strong efficacy after two months in PBS and demonstrating excellent biocompatibility. Compared to unmineralized hydrogels, the mineralized DN hydrogel exhibited superior mechanical strength, prolonged antimicrobial efficacy, and a reduced initial burst release. This study presents a novel strategy for optimizing AMP delivery, offering a multifunctional platform with exceptional potential for chronic wound healing and implant-associated infection prevention.

1. Introduction

Antimicrobial peptides (AMPs) are broad-spectrum agents with rapid bactericidal activity, low toxicity, and excellent biocompatibility, making them promising candidates for managing chronic wounds (*e.g.*, diabetic ulcers) and preventing implant-associated infections.[1–6] Unlike conventional antibiotics, AMPs exert their bactericidal effects by disrupting bacterial membranes, a mechanism that is less likely to induce drug resistance.[7] However, their clinical application is often hindered by rapid degradation and limited retention at the infection site.[8–10] To effectively counter persistent bacterial colonization and dynamic physiological stress in these environments, it is crucial to develop delivery systems that provide sustained antimicrobial activity while maintaining mechanical stability.

Hydrogels have been widely investigated as AMP delivery platforms due to their highwater content, biocompatibility, and tunable drug release properties.[11–19] Our group previously designed the potent AMP IK3,[20] which can self-assemble into a hydrogel that demonstrated exceptional antibacterial and anticancer activity and wound healing promotion in a mouse model. To further enhance the mechanical stability of the hydrogel, we developed a polyvinyl alcohol (PVA)/IK3 double-network (DN) hydrogel, which exhibited superior mechanical strength and durability compared to IK3 hydrogel.[21] However, in dynamic physiological environments such as chronic wounds or orthopedic implants, the AMP hydrogels still face challenges in sustained AMP retention and controlled release.[22,23] In chronic wounds, enzymatic degradation and fluid flow can rapidly deplete AMPs,[24] whereas in orthopedic applications, mechanical stress may lead to premature drug leakage.[25] These limitations demonstrate the need for advanced strategies to reinforce hydrogel stability and prolong antimicrobial activity.

Mineralization, inspired by natural biomineralization processes, presents a promising strategy to enhance the stability and controlled release of drugs in hydrogels.[26] The incorporation of inorganic materials, such as hydroxyapatite, into

[a] Shanghai Institute of Applied Physics, Chinese Academy of Sciences, Shanghai 201800, China. E-mail: zhangyi@sinap.ac.cn
[b] Institute of Materiobiology, College of Sciences, Shanghai University, Shanghai 200444, China
[c] University of Chinese Academy of Sciences, Beijing 100049, China

hydrogel networks can improve their structural integrity, modulate drug release profiles, and even impart intrinsic antimicrobial properties.[27–31] For example, Liu *et al.* developed a alendronate sodium (ADA) – mineralized hydrogel that mimicked natural dynamic biomineralization, demonstrated superior mechanical reinforcement, sustained ADA release, and enhanced bone repair efficacy compared to unmineralized hydrogels.[32] Wen *et al.* designed a biomimetic polyacrylic acid (PAA) – carboxymethyl chitosan (CMC) – dentin matrix (TDM) hydrogel, where TDM acts as a mineralization core template, enabling strengthened drug release, and osteoinductive properties, thereby promoting efficient *in situ* regeneration of hard tissue defects.[33] These findings highlight the potential of mineralization to synergistically improve both the mechanical and functional properties of hydrogels.

While previous studies explored mineralization for sustained drug release,[34–36] the potential of mineralization to precisely regulate the controlled release of AMPs from hydrogel had not been systematically investigated. Given that AMPs often suffered from rapid degradation and burst release,[37,38] incorporation mineralization into DN hydrogels offered a promising approach to overcoming these challenges. This method not only reinforced the mechanical stability of the hydrogel but also provided a diffusion-regulating barrier that enabled sustained and controlled AMP release, effectively addressing the limitations of existing AMP delivery strategies.

In this study, we developed a mineralized PVA/IK3 DN hydrogel system that integrates the advantages of both DN hydrogel technology and mineralization to achieve sustained release and enhanced antimicrobial activity. A systematic investigation of key mineralization parameters, including PVA concentration, IK3 loading, and salt ion concentration, revealed their effects on the release profiles of IK3 from the DN hydrogel. The results demonstrated that Ca/P elements incorporation not only improved the mechanical strength of the DN hydrogel but also optimized the controlled release of IK3, resulting in prolonged and effective antibacterial activity. Notably, the mineralized hydrogel maintained antimicrobial efficacy for over two months, highlighting its potential to advance AMP-based therapies for complex infection management.

2. Results and discussion

2.1 Characterization of mineralized DN hydrogels

In our previous study, we developed a DN hydrogel system by combining PVA with AMP IK3 (Fig. 1(A)). PVA was a biocompatible material that preserved the bioactivity of AMPs while enhancing the mechanical strength and durability of hydrogels.[39–41] To further improve the properties of the PVA/IK3 DN hydrogel, we induced mineralization to the hydrogel system by alternately immersed it in aqueous solutions of calcium chloride ($CaCl_2$) and sodium phosphate (Na_3PO_4), with each immersion lasting 60 s.[42] This process was repeated three times, resulting in the transformation of the initially transparent hydrogels into an opaque white color (Fig. 1(B) and (C)). The microstructure of the hydrogels is illustrated in Fig. 1(B) and (F). In the unmineralized DN hydrogels, a dense network of stacked nanofibers is observed. In contrast, the cross-sectional layer of the DN hydrogels mineralized with 100 μM salts exhibited a uniform distribution of microparticles, which are evenly dispersed throughout the hydrogel matrix. The size of the mineralized nanoparticles was 0.98 ± 0.13 μm. DN hydrogels mineralized with 50 and 500 μM salts show a sparser and less uniform distribution of mineral particles. Compared with the PVA-based hydrogels previously reported, the size of the mineralized nanoparticles varies, probably due to differences in mineralization conditions among different studies.[32,43] To further examine the composition of these particles, energy dispersive X-ray spectroscopy (EDS) was conducted (Fig. 1(G)). As anticipated, only trace amounts of calcium and phosphorus (2%) were detected in the unmineralized DN hydrogels. The DN hydrogels mineralized with 100 μM salts showed a significantly higher weight ratio of calcium and phosphorus, reaching 29.20%, compared to those mineralized with 50 μM and 500 μM salts, which exhibited Ca/P weight ratios of 20.84% and 14.91%, respectively (Table 1). The corresponding molar ratios of Ca and P in the mineralized DN hydrogels, which are shown in Table 2, are close to that of hydroxyapatite.[44] These findings confirm successful mineralization and demonstrate that salt concentration influences the degree of mineralization.

To further validate the EDS results and confirm the chemical composition and cross-linking within the hydrogels, Fourier Transform infrared spectroscopy (FTIR) characterization was conducted on both mineralized and unmineralized DN hydrogels. In both samples, characteristic absorption bands were observed, including a broad O–H stretching vibration around 3270 cm^{-1}, a C=O stretching vibration (amide I band) near 1630 cm^{-1}, a C–H bending vibration at approximately 1425 cm^{-1}, and a C–O stretching vibration around 1080 cm^{-1} (Fig. 1(H)). These results indicate the presence of PVA and peptide functional groups. After mineralization, a strong peak appeared at 560 cm^{-1}, corresponding to phosphate (PO_4^{3-}) bending vibrations, and a broader and more intense peak around 1030 cm^{-1} attributed to PO_4^{3-} stretching vibrations,[45] which overlapped with the C–O peak of PVA. These changes verify the successful incorporation of phosphate groups and the formation of ionic cross-links with Ca^{2+} ions. Furthermore, far-infrared (far-IR) analysis revealed a weak peak at approximately 260 cm^{-1} in the mineralized hydrogel,[46] potentially associated with Ca–O lattice vibrations, providing additional evidence of successful mineralization (Fig. 1(I)). Additionally, to investigate the internal crystalline structure of the hydrogels, X-ray diffraction (XRD) analysis was performed on both mineralized and unmineralized samples (Fig. 1(J)). Both hydrogels exhibited a diffraction peak at (101), corresponding to 2θ = 19.4° and 19.6°, which is characteristic of crystalline domains within PVA. In addition, the mineralized DN hydrogel displayed two extra diffraction peaks at 25.8° and 31.8°, corresponding to the (002) and (211) crystal planes of hydroxyapatite (HAp),[44] respectively. These results confirm the successful incorporation of crystalline HAp into

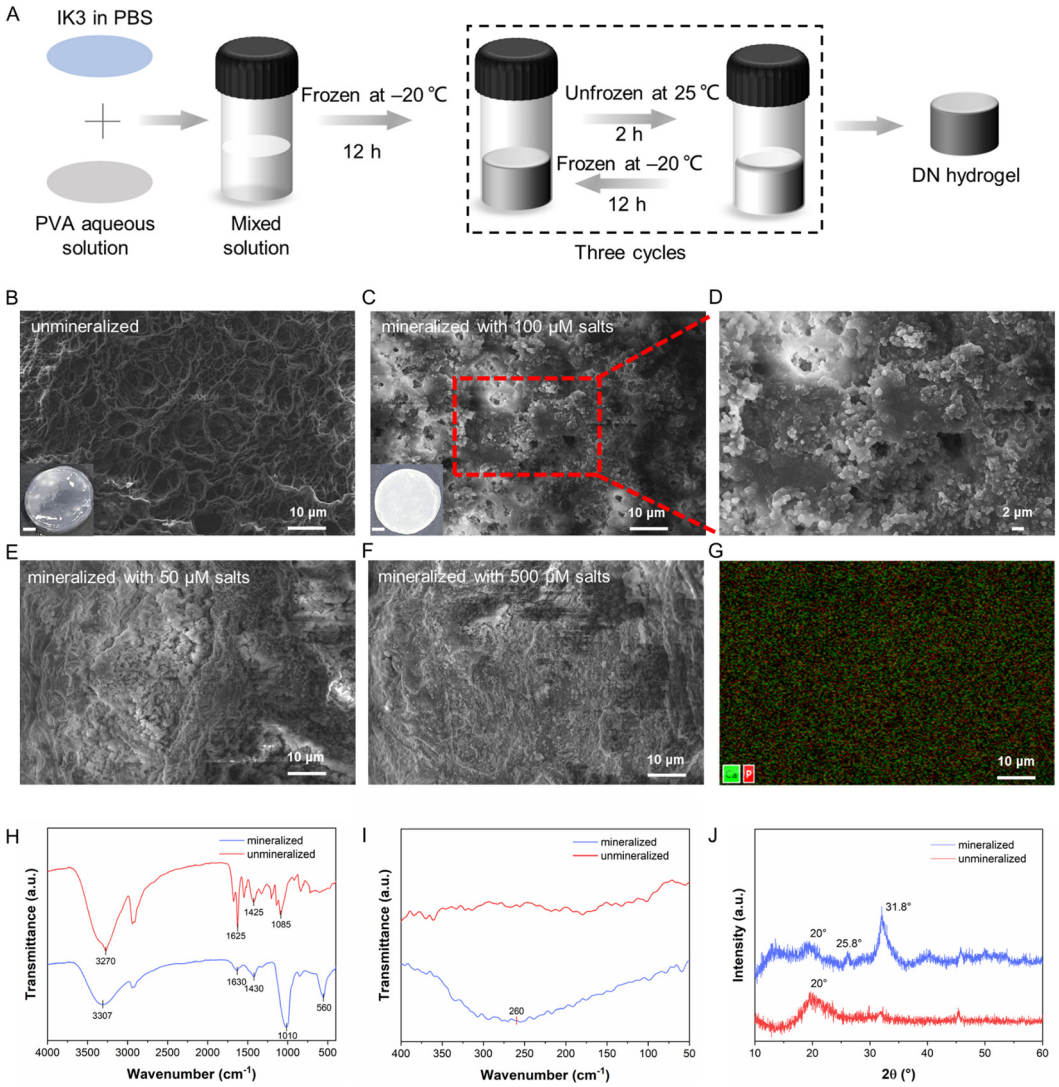

Fig. 1 (A) Schematic illustration of the hydrogel synthesis process. (B)–(F) SEM images of the cross-section of unmineralized and mineralized 4% PVA–1% IK3 DN hydrogels; insets in (B) and (C) show photographs of the unmineralized and mineralized DN hydrogels (scale bar: 2 mm). (G) EDS spectra indicating the presence of P and Ca elements in the region shown in (D). (H) and (I) FT-IR spectra of mineralized and unmineralized DN hydrogels. (J) XRD patterns of mineralized and unmineralized DN hydrogels.

Table 1 The element composition of unmineralized (Fig. 1(B)) and mineralized (Fig. 1(C), (E) and (F)) hydrogels

	wt%			
Element	Unmineralized	Mineralized with 50 μM salts	Mineralized with 100 μM salts	Mineralized with 500 μM salts
C	61.22	43.39	36.29	52.19
O	33.11	32.42	31.63	30.26
Na	1.61	1.21	0.50	0.95
P	0.82	6.48	9.40	4.28
Cl	2.08	2.14	2.38	1.69
Ca	1.16	14.36	19.80	10.63
Total content	100.00	100.00	100.00	100.00

Table 2 The molar ratios of Ca, P, and O elements in the DN hydrogels under different mineralization conditions

Mineralization condition	Molar ratio (Ca : P : O)
Unmineralized	1.1 : 1 : 77
Mineralized with 50 μM salts	1.7 : 1 : 9.7
Mineralized with 100 μM salts	1.6 : 1 : 6.5
Mineralized with 500 μM salts	1.9 : 1 : 13.7

the hydrogel matrix and indicate that the mineralized DN hydrogel possesses good crystallinity.

2.2 Effects of mineralization on the mechanical properties and swelling behavior of DN hydrogels

Rheological testing revealed that the mineralization process significantly enhanced the mechanical modulus of the DN hydrogels (Fig. 2). It was found that the mineralizing salt concentration had a significant impact on the mechanical modulus of the mineralized DN hydrogel. When the salt

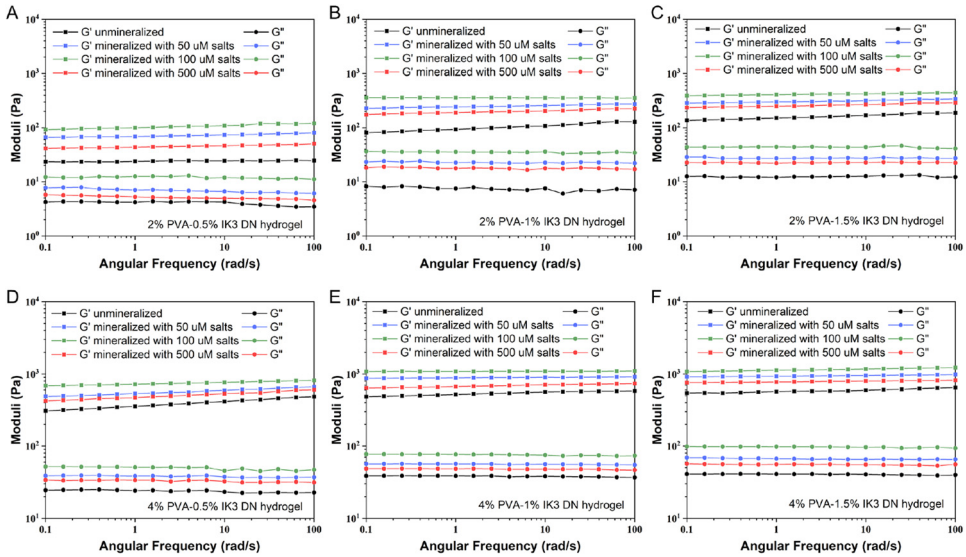

Fig. 2 The rheology study showing the evolution of the modulus of DN hydrogels, where mineralization was carried out with $CaCl_2$ and Na_3PO_4 (50 μM, 100 μM, or 500 μM for both salts). (A)–(F) Frequency sweep tests of the DN hydrogel. The sweep frequency varied from 0.1 to 100 rad s^{-1} at a strain of 1%.

concentration was 100 μM, the modulus of hydrogel was significantly higher than at other two concentrations (Fig. 2). The concentrations of gelators, PVA and IK3, also play a role on the mechanical modulus of the mineralized DN hydrogels. At a fixed PVA concentration of 2%, as the peptide concentration increased from a non-gel-forming state (that is, 0.5%) to a gel-forming state (1% or 1.5%), the modulus of the mineralized hydrogel showed a marked improvement (Fig. 2(A)–(C)). In contrast, above the gelation threshold of the peptide concentration, the modulus changed very slightly (Fig. 2(B) and (C)). Similar modulus variation trend is observed in the hydrogels in which the PVA concentration was 4% (Fig. 2(D)–(F)). In addition, the modulus of hydrogel containing 4% PVA was markedly higher than that containing 2% PVA (comparing Fig. 2(D) with Fig. 2(A), (E) with Fig. 2(B) and (F) with Fig. 2(C), respectively).

The mineralization outcome significantly impacted the swelling behavior of the DN hydrogel. As shown in Fig. 3(A)–(F), as the degree of mineralization increased (500 μM < 50 μM < 100 μM of $CaCl_2/Na_3PO_4$), the swelling ratio decreased substantially. This trend was consistent with the variation observed in modulus. This result suggests that mineralization created a densely organized microstructure within the hydrogel network, which reduced water penetration and limits volumetric expansion. Previous studies have demonstrated that the swelling behavior of PVA-based hydrogels strongly depends on the nature of the second network component. For examples,

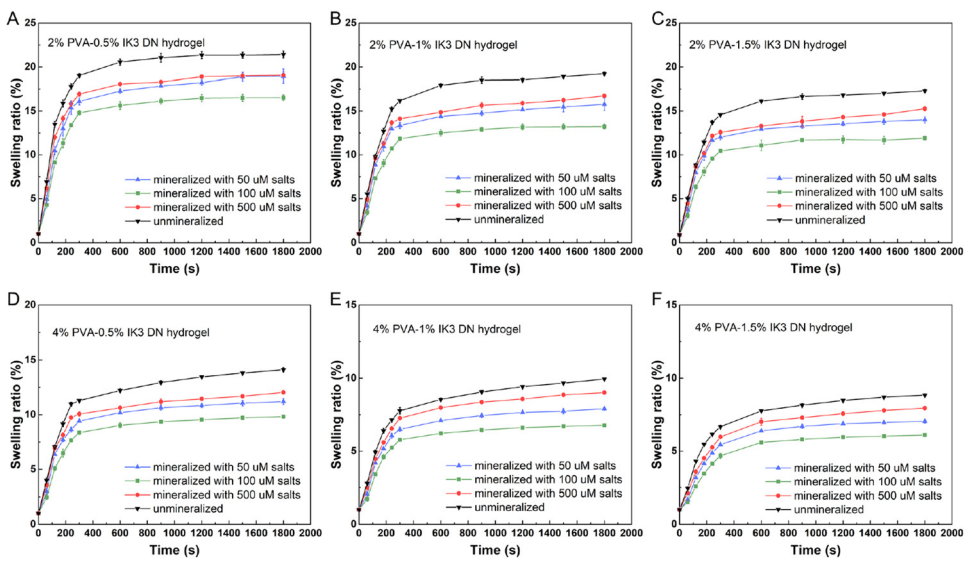

Fig. 3 (A)–(F) Swelling ratio of the DN hydrogels, where mineralization was realized with $CaCl_2$ and Na_3PO_4 (50 μM, 100 μM, and 500 μM for both salts). The swelling ratio of the hydrogels was measured in PBS at different time points.

PVA/PAAc-N^+ hydrogels and FC γ-PGA/PVA hydrogels exhibit ultra-low swelling ratios around 0.3% due to dense cross-linking and strong electrostatic interactions.[47,48] In contrast, GG/PVA hydrogels can reach swelling ratios as high as 20%, depending on their polymer composition and network structure.[49] In our system, the second network is composed of IK3 nanofibers, which are physically cross-linked and inherently possess relatively poor mechanical strength. When integrated with the PVA network, this design results in a moderate swelling degree, providing a balance between mechanical stability and sufficient water absorption.

2.3 Release behavior of mineralized DN hydrogels

The release behavior of AMPs from the mineralized and unmineralized DN hydrogels was systematically evaluated to assess the impact of mineralization on the sustained release profiles. The hydrogels were incubated in PBS at 37 °C, and the cumulative release of AMPs was monitored over time using UV-visible spectrophotometry.

The results demonstrated that the mineralization process markedly decreased the IK3 release rate from the hydrogel. In these experiments, the effects of three variables were systematically investigated, namely PVA concentration, IK3 concentration, and salt ion concentration. First, the effect of concentrations of $CaCl_2$ and Na_3PO_4 (either 50 μM, 100 μM, or 500 μM of both salts) on the release profile of IK3 from the DN hydrogel was investigated. It was found that the release performance of the AMP did not consistently improve with increasing salt ion concentrations (Fig. 4(A)–(F)). Under fixed concentrations of PVA and IK3, the DN hydrogels mineralized with 100 μM salts exhibited a most effective reduction in the IK3 release rate, probably due to that this salt concentration is suitable for developing a uniform and stable mineralization structure. In contrast, 50 μM salts might not sufficient to form such a mineralization structure in DN hydrogels, while 500 μM salts might contain the excessively high ion concentration that led to an uneven mineralized layer, compromising its structural uniformity and stability. These findings highlight the crucial role of salt ion concentration in forming a uniform, functional mineralized layer, which is vital for regulating AMP release performance.

Moreover, the impact of PVA concentration on the IK3 release rate was examined. Testing revealed that a 2% PVA concentration is the minimum threshold for hydrogel formation. Experimental results show that the IK3 release rate from the DN hydrogel formed with 2% PVA (Fig. 4(A)–(C)) is significantly higher than that from the hydrogel formed with 4% PVA (Fig. 4(D)–(F)). This is likely due to the relatively weaker network strength of the hydrogel formed with 2% PVA, resulting in insufficient restraint and consequently accelerating IK3 release.

In addition, the effect of IK3 concentration on sustained release performance was explored. Experimental results indicated that at a 0.5% IK3 concentration, the sustained release rate of IK3 (Fig. 4(A) and (D)) was significantly higher than those at concentrations 1% and 1.5%. This is likely due to IK3 existing and being released in an oligomeric form at this concentration, and the failure to form a complete DN hydrogel, as 1% is the minimum threshold required for IK3 hydrogel formation.[20] As the IK3 concentration increased to 1.5%, the release rate of IK3 from the mineralized DN hydrogel was slightly higher than that from the hydrogel formed with 1% IK3. This suggests that the initial IK3 concentration influences its release behavior. Higher IK3 concentrations likely result in a denser distribution within the hydrogel networks, thereby enhancing the concentration gradient and accelerating the diffusion release process (Fig. 4(E) and (F)). In this concentration range, the effect of the increased concentration gradient

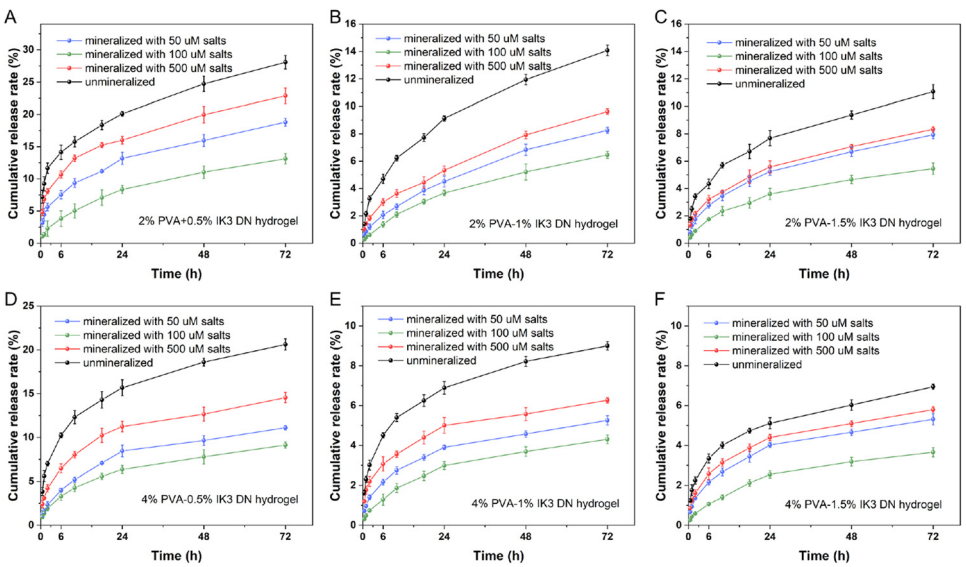

Fig. 4 (A)–(F) Cumulative release rate of IK3 from the DN hydrogels to PBS solutions. The mineralization of the PVA/IK3 DN hydrogels was carried out with $CaCl_2$ and Na_3PO_4 (50 μM, 100 μM, or 500 μM for both salts).

seems to outweigh the potential diffusional hindrance caused by network densification.

These findings collectively demonstrate that the concentrations of mineralizing salt ions, PVA, and the initial AMP content play critical roles in regulating the sustained release behavior of AMPs from mineralized DN hydrogels. The observed changes in hydrogel modulus were closely correlated with variations in the AMP release rate, suggesting that the incorporation of inorganic microparticles enhances the structural integrity of the hydrogel matrix. This mechanical reinforcement not only improves the hydrogel's stability but also provides a theoretical basis for tuning sustained release performance, thereby broadening the potential of mineralized DN hydrogels for advanced biomedical applications.

To further investigate the drug (IK3) release kinetics of the mineralized DN hydrogels, the Korsmeyer–Peppas model[50] was used to analyze the diffusion-controlled mechanism under various conditions. The fitting results show that the correlation coefficient (R^2) for the Korsmeyer–Peppas model is equal to 0.99 (Fig. 5), indicating that the model accurately describes the drug release behavior. The analysis shows that, for the unmineralized DN hydrogels or the DN hydrogels mineralized with other salt concentrations (50 or 500 μM), their diffusion exponents (n values) are less than 0.5 (Fig. 5), indicating that their release behavior follows Fickian diffusion. In contrast, for the DN hydrogels mineralized with 100 μM $CaCl_2$ and Na_3PO_4, the n values are generally greater than 0.5, indicating that drug release is controlled by both diffusion and polymer network relaxation, exhibiting a non-Fickian diffusion mechanism. Interestingly, the n value of the DN hydrogel composed of 4% PVA and 0.5% IK3, which was also mineralized with 100 μM salts, is below 0.5. This may be attributed to the IK3 concentration (0.5%) being below its critical gelation threshold (1%), which is insufficient to effectively form a double-network structure. Additionally, the increased PVA concentration (4%) results in a higher cross-linking density within the hydrogel network, reducing chain mobility. This combination yields a mechanically stronger hydrogel structure, leading to IK3 release that still follows Fickian diffusion.

The mineralization process significantly affected both the structure and release behavior of the DN hydrogel. At 50 and 500 μM salt concentrations, the micro-particles observed on the hydrogel cross-section appeared unevenly distributed, and the degree of mineral deposition was relatively low. The resulting mineralized layer may have provided only limited resistance to diffusion, allowing the drug to diffuse rapidly along the concentration gradient, exhibiting a Fickian diffusion mechanism. At a 100 μM salt concentration, the hydrogel cross-section appeared to exhibit a more uniform distribution of mineralized particles, with a relatively higher degree of mineral deposition. This denser mineralized structure may have increased the resistance to drug diffusion. Moreover, the presence of the mineralized structure might have simultaneously inhibited the network relaxation and swelling behavior of the hydrogel, leading to a deviation from classic Fickian diffusion and exhibiting characteristics of a non-Fickian diffusion mechanism. These findings suggested that the mineralization process significantly modulates the structural performance and sustained release properties of DN hydrogels by enhancing their mechanical modulus and suppressing their swelling behavior. These findings not only elucidate the mechanism by which mineralization affects the mechanical properties and swelling behavior of hydrogels but also provide a critical theoretical foundation for optimizing the overall performance of DN hydrogels.

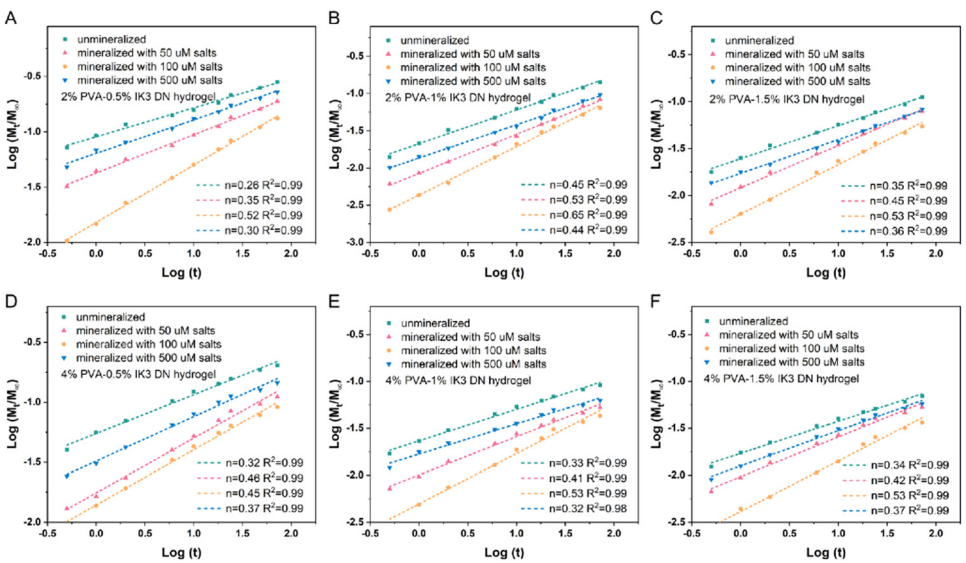

Fig. 5 (A)–(F) Korsmeyer–Peppas model analysis of the release kinetics of IK3 from the DN hydrogels to PBS solutions. The mineralization of the DN hydrogels was realized with $CaCl_2$ and Na_3PO_4 (50 μM, 100 μM, or 500 μM for both salts). Analysis of the IK3 release kinetics was carried out with different PVA concentrations, IK3 concentrations, and mineralizing salt concentrations.

2.4 Antibacterial activity of IK3 controllably released from the mineralized DN hydrogels

We systematically investigated the antibacterial activity of IK3 released from mineralized DN hydrogels. The concentrations of IK3 and PVA in the mineralized DN hydrogels used in the following experiments were 1% and 4%, respectively. The IK3 solution was collected at various time points when the hydrogel was soaked in PBS, and its antibacterial activity against *S. aureus* and *E. coli* was tested. As shown in Fig. 6(A) and (B), the results revealed significant temporal differences in antibacterial activity. The IK3 solution collected after 3 h of immersion of the unmineralized hydrogel in PBS killed approximately 90% of the bacteria in 3 h, achieving complete eradication of both *S. aureus* and *E. coli* after 6 h. In contrast, the IK3 solution collected after 3 h of immersion of the mineralized hydrogel in PBS exhibited a slower bactericidal activity, with about 40% of *S. aureus* and 50% of *E. coli* killed within 3 h; after 6 h, the bactericidal rates increased to approximately 63% for *S. aureus* and 68% for *E. coli*, achieving complete eradication only after 24 h. Additionally, almost all *S. aureus* and *E. coli* treated with the IK3 release solution collected from the unmineralized hydrogel after 6 h of immersion exhibited red staining, indicating bacterial cell membrane damage and subsequent cell death. In contrast, bacteria treated with IK3 release solutions collected from the mineralized hydrogel after 6 h of immersion exhibited both red and green staining. However, after 24 h of immersion, all bacteria treated with IK3 release solutions collected from the mineralized hydrogel displayed red staining, indicating cell death (Fig. 6(C) and (D)). These observations are consistent with the results obtained from the agar plate experiments.

The mineralization process significantly delayed the release rate of IK3, allowing the mineralized hydrogel to display more stable sustained-release characteristics and progressively improved antibacterial activity. In contrast, the unmineralized hydrogel, owing to the rapid release of IK3, efficiently killed bacteria within a short time. On the other hand, the mineralized hydrogel effectively controlled the concentration of released IK3, ensuring continuous antibacterial activity over 24 h while demonstrating superior sustained-release performance and antibacterial activity. These results demonstrated the importance of the mineralization process in optimizing the sustained-release properties of hydrogels. In further studies, both mineralized and unmineralized hydrogels were immersed in PBS for up to two months, and the antibacterial activity of their release solutions was evaluated. The results showed that after 48 h of immersion, the IK3 release from the mineralized hydrogel still effectively killed bacteria, while the antibacterial activity of the unmineralized hydrogel was almost completely lost (Fig. 7(A) and (B)). Furthermore, as shown in Fig. 7(C) and (D), after 48 h of immersion, bacteria treated with IK3 release solutions collected from mineralized hydrogels exhibited red staining, while those treated with IK3 release solutions from unmineralized hydrogels displayed green staining, consistent with the results observed in agar plate experiments. This finding further confirms that the mineralization process not only significantly prolonged the antibacterial activity of the hydrogel but also greatly enhanced its sustained-release performance. This controlled release characteristic not only effectively extended the antibacterial duration of the hydrogel but also enhanced its durability and stability for practical applications. Therefore, mineralization imparted excellent sustained-release properties to the DN hydrogel, maintaining high antibacterial activity over an extended period and supporting the long-term use of antibacterial materials.

In addition, it was found that the mineralized hydrogel lost its mass for ~12% during immersion in PBS in two months (Fig. 7(G)). Since the IK3 and PVA only accounted for a small

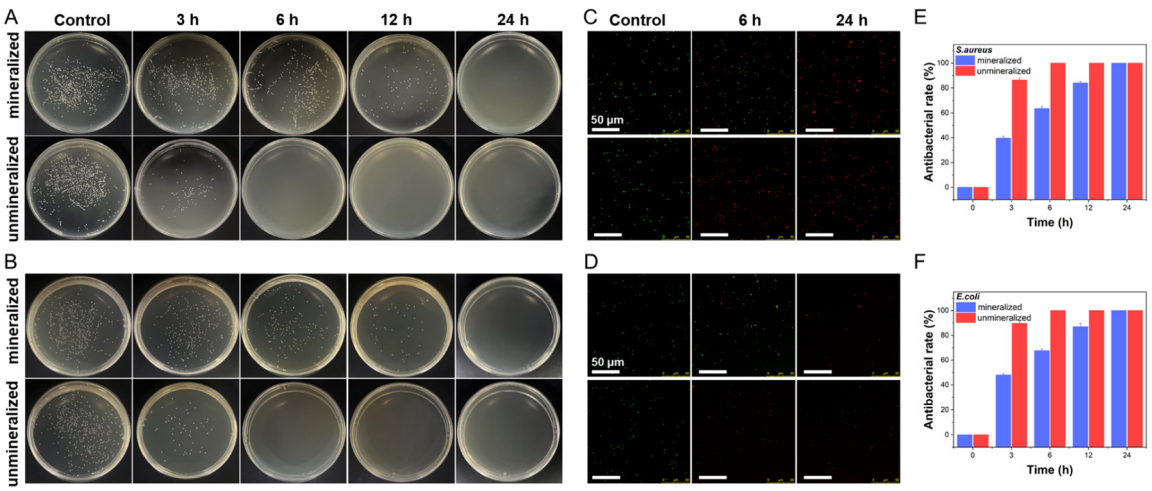

Fig. 6 Antibacterial activity of the IK3 release solution collected from the mineralized and unmineralized DN hydrogels, where mineralization was carried out with 100 μM $CaCl_2$ and 100 μM Na_3PO_4. (A) and (B) Antibacterial activity of the IK3 solution collected from the mineralized and unmineralized DN hydrogels against *S. aureus* (A) and *E. coli* (B) at different time points, determined by agar plate method. (C) and (D) Confocal microscopy images of *S. aureus* (C) and *E. coli* (D) treated with IK3 released from the mineralized and unmineralized DN hydrogels soaked in PBS for 0 h, 6 h and 24 h, respectively. (E) and (F) Quantitative statistics of antibacterial rates of *S. aureus* (E) and *E. coli* (F). Scale bar: 50 μm.

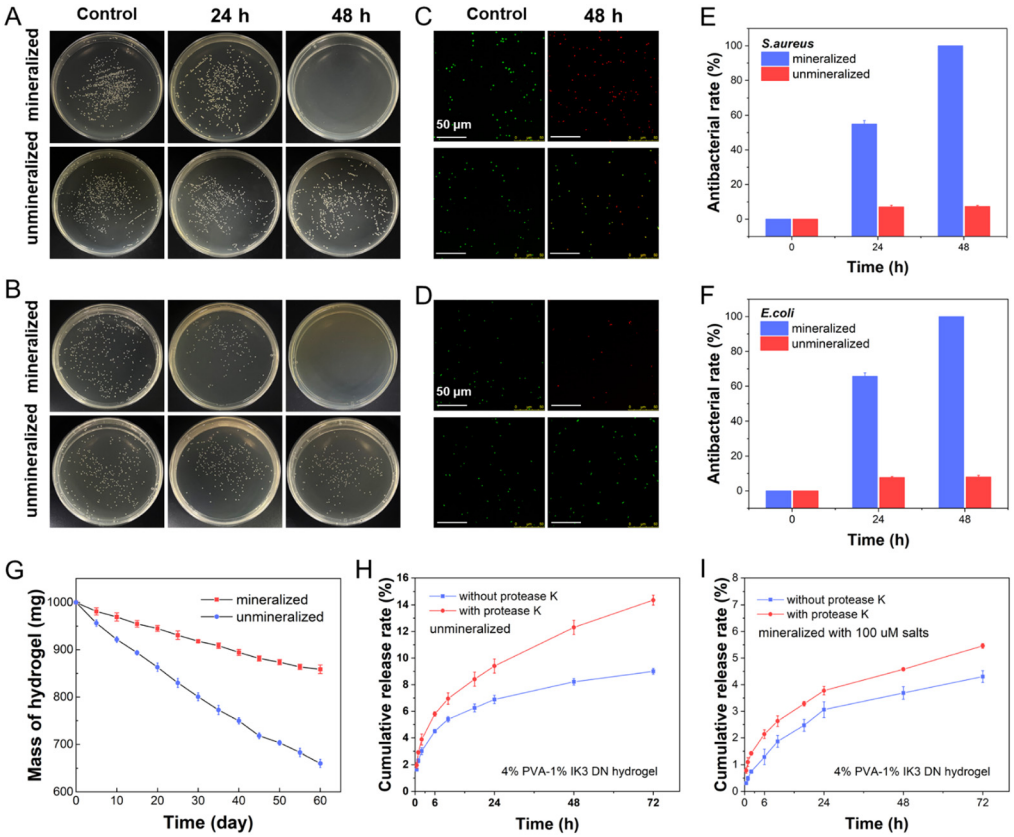

Fig. 7 Antibacterial activity of the IK3 release solution collected from the mineralized and unmineralized DN hydrogels, where mineralization was carried out with 100 μM $CaCl_2$ and 100 μM Na_3PO_4. (A) and (B) Antibacterial activity of the IK3 solution released from the mineralized and unmineralized DN hydrogels against *S. aureus* (A) and *E. coli* (B) at different time points, after immersion in PBS for up to two months, determined by agar plate method. (C) and (D) Confocal microscopy images of *S. aureus* (C) and *E. coli* (D) treated with IK3 release solutions from mineralized and unmineralized DN hydrogels, collected after immersion in PBS for two months at 0 h and 48 h, respectively. (E) and (F) Quantitative statistics of antibacterial rates of *S. aureus* (E) and *E. coli* (F). Scale bar: 50 μm. (G) Mass loss of mineralized and unmineralized DN hydrogels in PBS solution for up to two months, where mineralization was carried out with 100 μM $CaCl_2$ and 100 μM Na_3PO_4. (H) and (I) Cumulative release rate of IK3 from the DN hydrogels in the presence of protease K in PBS solutions.

share in the DN hydrogel, this mass loss indicates there was a slight degradation for the mineralized phase, a possible cause for the intriguing release behavior of the IK3 peptide from the mineralized DN hydrogels. In contrast, the unmineralized hydrogel showed a much significant mass loss (~35%) (Fig. 7(G)), partly due to the release of IK3 peptides and the subsequent erosion and dissolution of the PVA network during long-term exposure to PBS solution. Water would also release from the unmineralized hydrogel to PBS solution due to the gradient of salt concentrations.

To further assess degradation resistance of mineralization, we measured the release of IK3 peptide in the presence of protease K in PBS solutions. The results (Fig. 7(H)–(I)) show that protease K significantly accelerated IK3 release from unmineralized hydrogels (a cumulative release rate of 14.5% *versus* 9% in 72 h); in contrast, mineralized hydrogels were much less affected (a cumulative release rate of 5.5% *versus* 4.5% in 72 h). These results indicate that the mineralized phase serves as a protective barrier that limits enzyme penetration, thereby reducing enzymatic degradation of the hydrogel matrix and stabilizes the hydrogel networks.

2.5 Biocompatibility of the mineralized DN hydrogel

To assess the biocompatibility of mineralized and unmineralized DN hydrogels, MTT assays were performed on NIH 3T3 cells cultured with these hydrogels. The results demonstrated that after 24 h of co-culture, cell viability exceeded 90% for both mineralized and unmineralized hydrogels (Fig. 8(A)). These findings indicate that the hydrogels exhibit negligible cytotoxicity when cultured with NIH 3T3 cells over a short-term period. However, after 3 d of co-culture, a significant divergence in cell viability was noted. Cells co-cultured with the mineralized hydrogel exhibited significantly higher viability compared to the control group, while the viability of cells co-cultured with the unmineralized hydrogel was lower than that of the control group (Fig. 8(A)). Further results from Phalloidin and DAPI staining revealed that cells cultured with both mineralized and unmineralized hydrogels maintained intact cytoskeletal structures, with clear and undamaged nuclei, further confirming the absence of significant direct cytotoxicity from either hydrogel type (Fig. 8(B)). Additionally, live/dead staining of NIH 3T3 cells showed that after 72 h of co-culturing with the mineralized

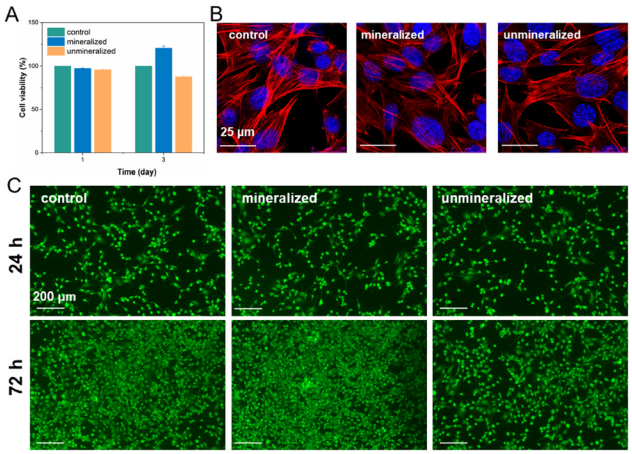

Fig. 8 Biocompatibility of the mineralized DN hydrogel, where mineralization was carried out with 100 μM $CaCl_2$ and 100 μM Na_3PO_4. (A) Cytotoxicity test of mineralized and unmineralized DN hydrogels after incubation for 1 and 3 d. (B), (C) Fluorescence images of NIH 3T3 cells stained with actin-tracker red-rhodamine and DAPI (B) and calcein-AM/PI (C), with PBS as the control group. The scale bars are 25 μm in (B) and 200 μm in (C), respectively.

hydrogel, cell density was significantly higher than in the control group, whereas the density of cells in the unmineralized hydrogel group was noticeably lower (Fig. 8(C)). These findings suggest that the low-concentration IK3 slowly released from the mineralized hydrogel significantly promotes NIH 3T3 cell proliferation, while the high-concentration IK3 released in a short time from the non-mineralized hydrogel inhibits cell proliferation. The mineralized hydrogel effectively controlled the release rate of AMPs through its sustained-release mechanism. This sustained-release mechanism not only ensured prolonged antibacterial efficacy but also established a favorable microenvironment for cellular activities, thereby enhancing cell proliferation and viability. These double-functional properties are particularly advantageous for biomedical applications such as wound healing, where sustained antibacterial activity and active cellular integration are critical for tissue regeneration.

3. Conclusion

In this study, we developed a mineralized PVA/IK3 DN hydrogel and systematically investigated the effects of PVA concentration, IK3 loading, and salt concentration on IK3 release profiles from the DN hydrogel. The findings revealed that the formation of a densely-packed inorganic microstructures through mineralization significantly enhanced the structural integrity and mechanical robustness of the DN hydrogel while regulating IK3 release kinetics that enables sustained and controlled release. *In vitro* antibacterial assays demonstrated that the mineralized DN hydrogel achieved long-term antibacterial efficacy through controlled IK3 release, maintaining excellent antibacterial activity even after two months of immersion in PBS, while also exhibiting outstanding biocompatibility. These results emphasize the critical role of mineralization in optimizing hydrogel performance and demonstrate its potential for biomedical applications such as wound healing. This study provides a promising strategy for designing advanced biomaterials with prolonged antibacterial protection and optimized cellular integration.

4. Experimental

4.1 Materials

IK3 peptides were synthesized by China Peptides Co., Ltd, with a purity of 99%, as confirmed by high-performance liquid chromatography (HPLC) and mass spectrometry (MS). The peptide powder was stored at −20 °C until use. Polyvinyl alcohol (PVA, 1750 ± 50, 99% purity, 99 wt% in water), sodium phosphate (Na_3PO_4), calcium chloride ($CaCl_2$), phosphate-buffered saline (PBS), dimethyl sulfoxide (DMSO), hydrochloric acid (HCl), sodium hydroxide (NaOH), and Luria–Bertani (LB) medium were obtained from Sinopharm Chemical Reagent (China). The LIVE/DEAD BacLight Bacterial Viability Kit (L13152, Molecular Probes) was purchased from Sigma-Aldrich (St. Louis, MO). Reagents including 3-(4,5-dimethylthiazol-2-yl)-2,5-diphenyl tetrazolium bromide (MTT), actin-tracker red-rhodamine, DAPI, calcein/PI cell viability and cytotoxicity detection kits were purchased from Beyotime Biotechnology (China). All aqueous solutions were prepared using deionized Milli-Q water (Millipore Corp., 18.2 MΩ cm at 25 °C).

4.2 Mineralized DN hydrogel formation

IK3 peptides were dissolved in Milli-Q water to prepare a stock solution with a concentration of 4% (w/v, the same below). 10 wt% PVA solution was prepared by dissolving PVA powder in Milli-Q water under stirring and heating (90 °C). The above-mentioned peptide and PVA solutions were mixed together in different ratios to obtain the designated peptide and PVA concentrations. The mixed solution was put into a −20 °C refrigerator to freeze for 12 h, followed by thawing for 2 h. The freezing–thawing process was repeated three times to form a DN hydrogel.

To form the mineralized layer, The gel was alternately dipped in sodium phosphate (Na_3PO_4) solutions at concentrations of 50, 100, and 500 μM for 60 s, followed by a rinse in pure water for 10 seconds. This was followed by immersion in calcium chloride ($CaCl_2$) solutions at the same concentrations for 60 s, with another rinse in pure water for 10 seconds. This alternating dipping procedure was repeated for a total of three cycles (n = 3). Following this process, a mineralized DN hydrogel was successfully formed.

4.3 Scanning electron microscopy

The mineralized and unmineralized DN hydrogels were characterized using a Carl Zeiss AG, LEO 1530VP scanning electron microscope (SEM). For sample preparation, the hydrogels were frozen, cut into 100 μm thick slices, placed onto clean silicon wafers, and then freeze-dried. A gold layers was applied to the sample surfaces for SEM imaging. Elemental analysis

of the samples was conducted using energy dispersive X-ray spectroscopy (EDS).

4.4 FTIR spectroscopy

After freeze-dried, the mineralized and unmineralized DN hydrogels were analyzed. FTIR spectra were recorded using a Bruker VERTEX 80v spectrometer equipped with an ATR accessory. Spectra in both mid-infrared and far-infrared regions were collected. The measurement range was set from 4000 to 5 cm^{-1}, with a resolution of 4 cm^{-1} and 32 scans per sample.

4.5 XRD analysis

After freeze-dried, the mineralized and unmineralized DN hydrogels were analyzed using XRD with a Bruker D8 Advance diffractometer. The measurement was performed at room temperature. The scanning range was set from 10° to 60° (2θ) with a step size of 0.02°.

4.6 IK3 release study

IK3 peptide solutions were prepared at varying concentrations, and the absorbance at 280 nm was measured using a UV-2600 spectrophotometer (Shimadzu, Japan) to generate a standard curve. For release studies, 100 μL of the DN hydrogel containing different concentrations of IK3 and PVA was placed in a vial, to which 2 mL of PBS was added. The samples were incubated for different time intervals, after which 1 mL of the supernatant was carefully collected for monitoring absorbance at 280 nm. The same procedure was conducted with a pure PVA hydrogel as the control, and the peptide concentration was determined by subtracting the absorbance of the pure PVA hydrogel from that of the DN hydrogel. The release profile of the IK3 peptide was calculated using the standard curve. To determine the effect of protease K on IK3 release, protease K was added to PBS to a concentration of 10 mg mL^{-1}, and the aforementioned procedure was repeated. The release kinetics were further analyzed by fitting the data to Korsmeyer–Peppas models.

$$\text{Korsmeyer} - \text{Peppas models: } \frac{M_t}{M_\infty} = Kt^n$$

where M_t refers the amounts of IK3 released at a specified time, M_∞ refers to the total amount of IK3 in the hydrogel, K stands for the release rate constant, and n denotes the diffusion index of the drug release mechanism.

4.7 Rheometry

The rheological analysis of the hydrogels was measured using a MCR302 (Anton Paar Austria) with a 25 mm aluminum parallel plate. Frequency scans (0.1–100 rad s^{-1}.) were performed using a constant stress of 1%. The storage modulus (G') and loss modulus (G'') of hydrogels were analyzed.

4.8 Swelling ratio

For the swelling experiment, equal weights (W_i) of hydrogels were placed into vials, and 1 mL of PBS was added. At predetermined time points, PBS was carefully removed, and the hydrogel was weighed (W_t) after gently blotting the surface with filter paper to remove excess water. The swelling ratio was then calculated using the following equation:

$$\text{Swelling ratio}(\%) = \frac{W_t - W_i}{W_i}$$

4.9 Antibacterial activity

S. aureus (CGMCC1.2386), *E. coli* (CGMCC1.2463) were acquired from the China General Microbiological Culture Collection Center (CGMCC). *S. aureus* and *E. coli* were revived and cultured to the logarithmic growth phase, then harvested and resuspended in saline to a final concentration of 1×10^8 CFU mL^{-1}. Release solutions from the hydrogels at different time points (100 μL) were added to each well, followed by the addition of 100 μL of the bacterial suspension and 1 mL of Luria–Bertani (LB) liquid medium. The mixture was incubated at 37 °C for 2 h. After incubation, the bacterial solution was serially diluted and spread onto LB agar plates for colony counting.

S. aureus and *E. coli* were resuspended in PBS to an OD_{600} of 0.5, then mixed with release solutions from the hydrogels at different time points and incubated at 37 °C for 1 h. The mixture (200 μL) was washed twice with PBS and then incubated in the dark at room temperature for 15 minutes using the LIVE/DEAD BacLight Bacterial Viability Kit. Fluorescence images were captured using a Leica SP8 Confocal Microscope with an Olympus 60× oil immersion objective lens.

4.10 Biocompatibility

MTT assay was performed to assess the cytocompatibility of hydrogels in NIH 3T3 cell culture. Briefly, 100 μL of mineralized or unmineralized DN was placed into a 96-well plate. NIH 3T3 cells were seeded on the hydrogel surfaces at a density of 5×10^3 cells per well and cultured for 24 or 72 h at 37 °C. Subsequently, 20 μL of MTT (5%) was added to each well and incubated for 4 h. The culture supernatants were carefully removed, and 150 μL of DMSO was added to dissolve the formazan crystals. The mixtures were stirred for 10 minutes in the dark. The absorbance at 495 nm was measured using a microplate reader. Cells without treatment were used as controls.

To evaluate cell viability and cytotoxicity, a calcein-AM/PI assay was performed. NIH 3T3 cells were cultured in growth medium (DMEM, 10% heat-inactivated fetal bovine serum) at 37 °C. For the assay, a cell suspension at a density of 1×10^5 cells per well was plated onto sterile 35 mm confocal dishes coated with mineralized and unmineralized DN hydrogels and incubated for 24 or 72 h. The calcein-AM/PI cell viability/cytotoxicity assay kit was added to the wells and incubated for 15 min, followed by washing with PBS to remove excess dye. Fluorescence images were acquired using a Leica SP8 confocal microscope (Germany) with an Olympus 10× oil immersion objective lens. In control groups, PBS replaced the mineralized and unmineralized DN hydrogels.

The sterile 35 mm confocal dishes were coated with mineralized or unmineralized DN hydrogels. A cell suspension (1×10^5 cells per well) was plated on the hydrogel surfaces and incubated for 72 h. Following incubation, the cells were gently

washed three times with PBS. The cells were then fixed with 4% paraformaldehyde solution (Beyotime Biotechnology, China) for 30 minutes at 37 °C. After fixation, the cells were washed 3 times with PBS containing 0.1% Triton X-100 for 5 minutes each. The cytoskeleton was stained with actin-tracker red-rhodamine (Beyotime Biotechnology, China) for 1 h, and the nucleus was stained with DAPI (Beyotime Biotechnology, China). Excess dye was removed by washing with PBS containing 0.1% Triton X-100 3 times. In the control group, cells were cultured in wells without hydrogel. Fluorescence images were captured using a Leica SP8 Confocal Microscope with an Olympus 10× oil immersion objective lens.

Conflicts of interest

The authors declare no conflict of interest.

Data availability

All data are available in the main text. Additional data related to this paper may be requested from the authors.

Acknowledgements

This work was supported by the National Key R&D Program of China no. 2022YFA1603601 and National Natural Science Foundation of China (no. 11975297 and 22393934). The authors gratefully acknowledge Prof. Yuan Qian and Dr Hailong Huang at Shanghai Institute of Applied Physics, CAS for the helpful discussion and suggestions on the experiments. The authors thank the staffs from BL06B beamline at Shanghai Synchrotron Radiation Facility for the assistance in IR measurement.

Notes and references

1 J. Wang, X. Dou, J. Song, Y. Lyu, X. Zhu, L. Xu, W. Li and A. Shan, *Med. Res. Rev.*, 2019, **39**, 831–859.
2 N. Mookherjee, M. A. Anderson, H. P. Haagsman and D. J. Davidson, *Nat. Rev. Drug Discovery*, 2020, **19**, 311–332.
3 C. Zhong, L. Zhang, L. Yu, J. Huang, S. Huang and Y. Yao, *BIO Integr.*, 2020, **1**, 156–167.
4 E. D. Freitas, R. A. Bataglioli, J. Oshodi and M. M. Beppu, *Colloids Surf., B*, 2022, **217**, 112693.
5 B. Thankappan, A. Thomas, A. Sakthivadivel, N. Shanmuganathan and J. Angayarkanni, *Colloids Surf., B*, 2023, **226**, 113331.
6 Z. Sun, L. Ma, X. Sun, A. J. Sloan, N. M. O'Brien-Simpson and W. Li, *Aggregate*, 2023, **4**, e309.
7 Q.-Y. Zhang, Z.-B. Yan, Y.-M. Meng, X.-Y. Hong, G. Shao, J.-J. Ma, X.-R. Cheng, J. Liu, J. Kang and C.-Y. Fu, *Mil. Med. Res.*, 2021, **8**, 48.
8 Z. Lai, X. Yuan, H. Chen, Y. Zhu, N. Dong and A. Shan, *Biotechnol. Adv.*, 2022, **59**, 107962.
9 X. Chen, J. Han, X. Cai and S. Wang, *Biotechnol. Adv.*, 2022, **60**, 108012.
10 C. Wang, C. Shao, Y. Fang, J. Wang, N. Dong and A. Shan, *Acta Biomater.*, 2021, **124**, 254–269.
11 J. Zhou, H. Zhang, M. S. Fareed, Y. He, Y. Lu, C. Yang, Z. Wang, J. Su, P. Wang, W. Yan and K. Wang, *ACS Nano*, 2022, **16**, 7636–7650.
12 S. M. Coulter, S. Pentlavalli, Y. An, L. K. Vora, E. R. Cross, J. V. Moore, H. Sun, R. Schweins, H. O. McCarthy and G. Laverty, *J. Am. Chem. Soc.*, 2024, **146**, 21401–21416.
13 H. Liu, X. Wei, H. Peng, Y. Yang, Z. Hu, Y. Rao, Z. Wang, J. Dou, X. Huang, Q. Hu, L. Tan, Y. Wang, J. Chen, L. Liu, Y. Yang, J. Wu, X. Hu, S. Lu, W. Shang and X. Rao, *Adv. Mater.*, 2024, **36**, 2412154.
14 Y. Tian, Y. Hou, J. Tian, J. Zheng, Z. Xiao, J. Hu and Y. Zhang, *J. Mater. Chem. B*, 2024, **12**, 8122–8132.
15 S. H. Jeong, S. Cheong, T. Y. Kim, H. Choi and S. K. Hahn, *ACS Appl. Mater. Interfaces*, 2023, **15**, 16471–16481.
16 Y. Zhang, Y. Gao, J. Wang, R. Gao, Q. Su, J. Zhang, L. Jiang, C. Zhang, P. Huang, W. Wang and Z. Feng, *Adv. Funct. Mater.*, 2024, **34**, 2312772.
17 H. Gong, X. Wang, X. Hu, M. Liao, C. Yuan, J. R. Lu, L. Gao and X. Yan, *Biomacromolecules*, 2024, **25**, 1602–1611.
18 H. Sun, X. Fu, C. Yang, C. Yuan and X. Yan, *Curr. Opin. Colloid Interface Sci.*, 2024, **73**, 101828.
19 Y. Liu, H. Gong, Z. Wang, C. Yuan, J. Lu and X. Yan, *Adv. Funct. Mater.*, 2023, **33**, 2305726.
20 Y. Hou, T. Tan, Z. Guo, Y. Ji, J. Hu and Y. Zhang, *Biomater. Sci.*, 2022, **10**, 3831–3844.
21 Y. Hou, Y. Tian, J. Tian, J. Shi, H. Zhao, J. Hu and Y. Zhang, *ACS Appl. Mater. Interfaces*, 2023, **15**, 29927–29938.
22 A. Copling, M. Akantibila, R. Kumaresan, G. Fleischer, D. Cortes, R. S. Tripathi, V. J. Carabetta and S. L. Vega, *Int. J. Mol. Sci.*, 2023, **24**, 7563.
23 L. Shang, J. Liu, Y. Wu, M. Wang, C. Fei, Y. Liu, F. Xue, L. Zhang and F. Gu, *ACS Appl. Mater. Interfaces*, 2023, **15**, 26273–26284.
24 H. Haidari, L. Melguizo-Rodríguez, A. J. Cowin and Z. Kopecki, *Am. J. Physiol.: Cell Physiol.*, 2022, **324**, C29–C38.
25 B. Costa, G. Martínez-de-Tejada, P. A. C. Gomes, M. C. L. Martins and F. Costa, *Pharmaceutics*, 2021, **13**, 1918.
26 S. Yao, B. Jin, Z. Liu, C. Shao, R. Zhao, X. Wang and R. Tang, *Adv. Mater.*, 2017, **29**, 1605903.
27 L. Wang, W. Zhao, Y. Zhao, W. Li, G. Wang and Q. Zhang, *Theranostics*, 2023, **13**, 673–684.
28 A. I. Robby, J.-H. Yang, E.-J. Jin and S. Y. Park, *Adv. Funct. Mater.*, 2024, **34**, 2402367.
29 S. Kim, A. U. Regitsky, J. Song, J. Ilavsky, G. H. McKinley and N. Holten-Andersen, *Nat. Commun.*, 2021, **12**, 667.
30 L. Xu, H. Kang, W. Wei, T. Goto, X. Wu and H. Dai, *Adv. Funct. Mater.*, 2024, **34**, 2406367.
31 R. Sun, Q. Zhang, C. Yu, Y. Zhu, Y. Zheng, T. Gu, L. Ye, W. Yang, X. Ying, Y. Xu, S. Fan, R. Tang, W. Qi and S. Yao, *Adv. Funct. Mater.*, 2024, **34**, 2408249.
32 J. Liu, X. Zhang, C. Xiao and X. Chen, *Adv. Funct. Mater.*, 2024, **34**, 2311844.
33 B. Wen, Y. Dai, X. Han, F. Huo, L. Xie, M. Yu, Y. Wang, N. An, Z. Li and W. Guo, *npj Regener. Med.*, 2023, **8**, 11.

34 P. Xiao, J. Liu, C. Du, S. Cheng, S. Liu, J. Liu, J. Zhan, Z. Chen, Y. Yang, Y. Lei, W. Huang and C. Zhao, *J. Controlled Release*, 2025, **380**, 240–255.
35 Y. Ding, Y. Mu, Y. Hu, J. Liu, C. Su, X. Sun, X. Chen, N. Jia and C. Feng, *J. Colloid Interface Sci.*, 2024, **656**, 1–14.
36 S. Liu, F. Han, P. Chen, R. Zhang and Y. Tao, *Carbohydr. Polym.*, 2025, **355**, 123354.
37 Z. Lai, X. Yuan, H. Chen, Y. Zhu, N. Dong and A. Shan, *Biotechnol. Adv.*, 2022, **59**, 107962.
38 R. E. W. Hancock, M. A. Alford and E. F. Haney, *Nat. Rev. Microbiol.*, 2021, **19**, 786–797.
39 S. G. Jin, *Chem. – Asian J.*, 2022, **17**, e202200595.
40 H. Li, C. Wu, X. Yu and W. Zhang, *J. Mater. Res. Technol.*, 2023, **24**, 2279–2298.
41 Y. Zhong, Q. Lin, H. Yu, L. Shao, X. Cui, Q. Pang, Y. Zhu and R. Hou, *Front. Chem.*, 2024, **12**, 2296–2646.
42 T. Nonoyama, S. Wada, R. Kiyama, N. Kitamura, M. T. Mredha, X. Zhang, T. Kurokawa, T. Nakajima, Y. Takagi, K. Yasuda and J. P. Gong, *Adv. Mater.*, 2016, **28**, 6740–6745.
43 J. Zhang, Y. Wang, J. Zhang, I. M. Lei, G. Chen, Y. Xue, X. Liang, D. Wang, G. Wang, S. He and J. Liu, *Small*, 2022, **18**, 2201796.
44 B. Xu, P. Zheng, F. Gao, W. Wang, H. Zhang, X. Zhang, X. Feng and W. Liu, *Adv. Funct. Mater.*, 2017, **27**, 1604327.
45 L. Hao, A. Wang, J. Fu, S. Liang, Q. Han, Y. Jing, J. Li, Q. Li, S. Bai, P. H. Seeberger and J. Yin, *Colloids Surf., A*, 2023, **657**, 130622.
46 N. O. Eddy, J. Oladede, I. S. Eze, R. Garg, R. Garg and H. Paktin, *Results Eng.*, 2024, **24**, 103374.
47 D. Zheng, C. Zhang, Z. Chen, P. Zhu and C. Gao, *J. Appl. Polym. Sci.*, 2023, **140**, e53792.
48 P. Ma, W. Liang, R. Huang, B. Zheng, K. Feng, W. He, Z. Huang, H. Shen, H. Wang and D. Wu, *Adv. Mater.*, 2024, **36**, 2305400.
49 C. Wang, Y. Jiang, Q. Ji, Y. Xing and X. Ma, *J. Cleaner Prod.*, 2024, **435**, 140503.
50 P. Trucillo, *Processes*, 2022, **10**, 1094.